Combined Effect of Porosity and Surface Chemistry on the Electrochemical Reduction of Oxygen on Cellular Vitreous Carbon Foam Catalyst

Jimmy Encalada, Keerthi Savaram, Nikolina A Travlou, Wanlu Li, Qingdong Li, Clara Delgado-Sánchez, Vanessa Fierro, Alain Celzard, Huixin He, Teresa J Bandosz

Combined Effect of Porosity and Surface Chemistry on the Electrochemical Reduction of Oxygen on Cellular Vitreous Carbon Foam Catalyst

Jimmy Encalada,[1] Keerthi Savaram[2], Nikolina A. Travlou[3], WanLu Li[3], Qingdong Li[2], Clara Delgado-Sánchez,[4] Vanessa Fierro,[4] Alain Celzard,[4] Huixin He[2] and Teresa J. Bandosz[1, 3,]*

[1] Department of Chemistry, The City College of New York, 160 Convent Ave, New York, 10031, USA

[2] Department of Chemistry, Rutgers University, 73 Warren Street, Newark, NJ 07102, USA

[3] Ph.D. Program in Chemistry, The Graduate Center of the City University of New York, New York, NY 10016

[4] Institut Jean Lamour, UMR Université de Lorraine – CNRS n°7198. ENSTIB, 27 rue Philippe Séguin, BP 21042, 88051 Epinal cedex 9, France

ABSTRACT: A new mechanism of O_2 reduction, which follows different principles than those generally accepted for describing ORR reduction on heteroatom-doped carbons, is suggested. It is based on the ability of oxygen to strongly adsorb in narrow hydrophobic pores. In this respect, a cellular vitreous carbon foam – graphene oxide composite was synthesized. The materials were doped with sulfur and nitrogen and/or heat-treated at 950^{o}C in order to modify their surface chemistry. The resultant samples presented a macro/microporous nature and were tested as ORR catalysts. To understand the reduction process, their surface was extensively characterized from the texture and chemistry points of view. The treatment applied markedly changed the volumes of small micropores and the surface hydrophilicity/polarity character. The results showed that the electron transfer number was between 3.87-3.96 and onset potential reached 0.879 V for the best performing sample. It is noteworthy that the best performing sample has the highest volume of pores smaller than 0.7 nm while no heteroatom doping. The hydrophobicity and the strong adsorption forces provided by these pores to pull oxygen inside are the possible reasons for the observed excellent performance. A decrease in the volume of these pores resulted in a decrease in the catalytic performance. When the surface was modified with heteroatoms, the performances further worsened because of the induced hydrophilicity.

KEYWORDS: *O_2 reduction, carbon, electrocatalysis, porosity, surface chemistry, specific interactions*

1. INTRODUCTION

Oxygen reduction reaction, ORR, is of significant importance for the development of new sources of energy.[1,2] So far, platinum carbon cathodes are considered as the best catalysts for this process. Nevertheless, they exhibit certain drawbacks including the high cost of Pt, a low tolerance to fuel/methanol crossover, and poor operation durability. All of these direct the attention of researchers to the development of non-noble metal or non-metal electrocatalysts, which could have a sufficient performance in ORR and could be used as replacement for Pt/C materials.[3-16] Non-metal electrocatalysts are mainly based on heteroatom-doped carbons.[13-15,17-25] So far, research efforts have focused on nonporous carbonaceous catalysts such as graphene oxide or graphene.[3,4,6-9,11,16] To increase the efficiency of the process, nitrogen,[5,6,8,10,13,14,23] sulfur,[7,9,11,15,24,25] phosphorus,[18,21,22] boron,[21,26] either alone or co-doped,[15,17] have been introduced into the carbon matrix. They have been indicated as providing catalytic active sites for oxygen electrosorption and reduction.[3,9,11,17,26]

Doping with nitrogen has been identified as bringing the highest number of electron transfer (n), high density of kinetic currents (J_k), and/or low onset potentials.[13,27] On N-doped carbons, n close to $4e^-$ and kinetic current reaching 4 mA cm^{-2} ($n = 3.96e^-$ and $J_k = 4.02$ mA cm^{-2} at -0.50 V vs. SCE (0.51 V vs. RHE)) have been reported.[27] Interestingly, on polyaniline-derived N- and O-doped mesoporous carbons, the shift in the onset potential to more positive value with respect to Pt was found with a kinetic current density reaching ~29 mA cm^{-2}, even though the reported n value was only $2.7e^-$.[13] This good performance was attributed to nitrogen groups in pyridinic configuration.

Another heteroatom used to dope carbons in order to improve their catalytic performance is sulfur.[24, 25] Besides providing catalytic centers for oxygen reduction, sulfur species might also attract oxygen. Reduced sulfur groups (in bisulfides and thiophenic configurations), when

located in very small pores, were found to help to withdraw oxygen from water/electrolyte.[24,25,28,29] These oxygen molecules are then strongly adsorbed in the pores whose width is similar to the size of O_2 molecules. This probably happens due to their surface hydrophobicity and overlapped adsorption potential. Other sulfur species, such as sulfoxide and sulfones, on the other hand, can promote a transport of aqueous electrolyte (with dissolved oxygen) to the small pores where oxygen reduction is enhanced. Their hydrophilicity and their probable existence in larger pores only are crucial assets for this process.

Even though doping solely with nitrogen or sulfur can certainly improve the performances of carbon, co-doping with both heteroatoms was reported to bring even better results. On S- and N-co-doped graphitic microporous carbon nanospheres, n = 3.8e^- and J_k = 27.0 mA cm^{-2} at -0.70 V vs. Ag/AgCl (0.28 V vs. RHE) were recorded.[15] On mesoporous co-doped graphene (S and N), n = 3.3e^- and J_k = 24.5 mA cm^{-2} at -0.50 V vs. Ag/AgCl (0.48 V vs. RHE) were associated to the synergy of charge and spin densities.[9] In the majority of those studies on applications of carbons as ORR catalysts, their performances have been reported as lower than those of Pt/C in terms of the desired 4e^- electron pathway and onset potential for fuel cell applications.[30] Nevertheless, contrary to Pt/C, they show a high tolerance to methanol crossover.[9,11,27]

There are not many studies on applications of highly porous carbon materials as ORR reduction catalysts.[13,24,25] These specific materials were even not mentioned in the recent review by Dai and co-workers.[31,32] It is well-known that a high porosity is beneficial for the dispersion/distribution of heteroatoms on the surface, and most studies so far have focused on this aspect.[24,25,28,29] Sung and coworkers[33] studied the role of predefined porosity in ORR catalytic site formation in Fe- and N-co-doped carbons. Even though the catalytic activity was mainly linked to Fe—N-C sites in the carbon matrix, the developed porosity promoted enhanced

ORR activity by contributing to the high dispersion of active sites. Porous carbon was investigated as a support for Au nanoparticles, and the obtained results of ORR activity were comparable to those on commercial 20% Pt/C. [34] The porosity in a carbon material also improved the distribution of Pt catalytic centers on the surface and thus increased their efficiency with respect to ORR.[35] The effects of porosity on the oxygen reduction on Pt-free carbon-based catalysts containing nitrogen, iron and zinc was investigated by Yin and coworkers.[36] They found that optimized porosity facilitated mass transport and thus enhanced fuel cell performances.

Recently, it has been indicated that porosity is not only important for dispersing active metal-containing centers, but also promotes in a very specific way the high ORR catalytic activity of hydrophobic microporous metal-free carbon materials.[37] On these carbons at the potential of 0.18 vs RHE, *n* reached 4 and kinetic current - 35 mA cm^{-2}, and an onset potential of 0.822 V. vs RHE was recorded. Interestingly, these materials had only traces of nitrogen and less than 10 at. % of oxygen, mainly in epoxy groups. Moreover, a dependence of the kinetic current on the volume of pores smaller than 0.7 nm, where oxygen can be strongly adsorbed, was found.

An interesting approach explaining the activity of pure carbon nanocages was proposed by Hu and co-workers.[38] Combining experiments with theoretical calculations, they found that intrinsic carbon defects, born in the carbon matrix, contribute to the observed enhanced ORR activity, irrespective to the presence of nitrogen. They suggested that zigzag edge defects or pentagon defects provide the catalytic activity for ORR, and the number of these defects might be increased in heteroatom-doped carbons. In their most active carbon, not only pores with sizes less than 1 nm were present but also a high volume of pores with sizes of about 10 nm was detected. High surface area was linked to the existence of intrinsic defects and thus to the high

ORR activity. Nevertheless, the electron transfer number was only 2.9. The role of carbon catalyst geometry for ORR was also investigated by Dai and co-workers.[39] Although they addressed N- and Fe-doped CNT/graphene complexes, their research suggested that unzipped walls of nanotubes provided the catalytic activity and that the charge transport was facilitated due to the intact electrical conductivity of the CNT/graphene. Those unzipped fragments, referred to by the authors as graphite oxide pieces, provided abundant edges and defect sites enhancing ORR catalytic activity.

To challenge the general belief that doping with nitrogen or sulfur makes the surface of carbon most active for ORR and to further evaluate the combined role of porosity for this process, cellular vitreous carbon foams of high volumes of micropores and macropores, as such and chemically modified, were evaluated as ORR catalysts. They were obtained by frothing aqueous solutions of biosourced phenolic resins, followed by polymerization of the resultant liquid foams and subsequent pyrolysis at 900°C.[40] The presence of large pores made it possible to impregnate these foams with graphene oxide (GO) in order to modify both porosity and surface chemistry. To further alter surface chemistry, S and N heteroatoms were introduced. An advance compared to state-of-the-art in the field is demonstrating that ORR is enhanced by adsorption process, and that hydrophobic pores of small sizes are crucial features of the catalysts. Having this in mind, we also provide further insight into the way heteroatoms and their specific forms existing inside the pore structure affect the ORR process. The materials were extensively characterized to link their catalytic behavior to the target surface features.

2. EXPERIMENTAL SECTION

2.1. Materials

Cellular vitreous carbon foam was prepared as described in Ref. 40 and 41. Briefly, a 40 wt. % aqueous solution of tannin extract, a plant-derived polyphenol, was prepared to which a crosslinker (hexamine), a polymerization catalyst (pTSA) and a surfactant (Cremophor® ELP) were added. The resultant, brown homogeneous solution was vigorously stirred with a blade mixer until a thick, viscous and stable liquid foam was obtained. The latter was hardened in an oven at 85°C for 24h then dried at room temperature for a few additional days. Finally, the rigid thermoset foam that was recovered was pyrolyzed at 900°C in a flow of very pure nitrogen, leading to a cellular monolith made of vitreous carbon. Due to the similarity of such process with the recipe of the meringues, according to which egg whites are whipped until stiff and then hardened in an oven, this special kind of carbon foam was called "carbon meringue",[41] and referred to as CM in the following discussion.

Graphite oxide (GO) was prepared using the Hummers method.[42] 0.555 grams of GO was sonicated for an hour and combined with 4.00 grams of CM. The mixture was further sonicated for another hour. Then the sample was filtered and dried at 120^{o}C. The composite is referred to as CMGO. It contains 90% CM and 10% GO.

In order to introduce nitrogen into CM, the sample was mixed with dicyandiamide at a ratio of 1:1. Then the mixture was heated in a horizontal furnace at 950^{o}C at a heating rate of 10^{o}C min^{-1} in a flow (100 mL min^{-1}) of nitrogen for 1 hour. The modified sample is referred to as CMN.

To prepare the carbon composites with sulfur, 2 g of CM or CMGO were placed in a horizontal furnace and exposed to 1000 ppm H_2S in nitrogen at a flow rate of 100 mL min^{-1}. The heating rate was 10^{o}C min^{-1}, final temperature 950^{o}C and dwell time 1 hour. The samples after that treatment are referred to as CM-S or CMGO-S, respectively. We arbitrarily decided to investigate to a greater extent the effect of oxygen in the carbon matrix on the surface chemistry,

thus on the catalytic behavior of sulfur-doped materials. The effect of nitrogen on the catalytic behavior of ORR carbon-based catalyst is well described in the literature, and only modification of the initial sample, CM, towards introduction of some N-containing groups was carried out.

CM and CMGO were also heat-treated for one hour at 950°C, with a heating rate of 10°C min^{-1} under 100 mL min^{-1} of nitrogen. The corresponding samples are referred to as CM-H and CMGO-H, respectively.

The preparation steps are illustrated in Figure 1. For reference, Pt/Vulcan catalytic carbon with 20 wt. % platinum (Sigma Aldrich) was used.

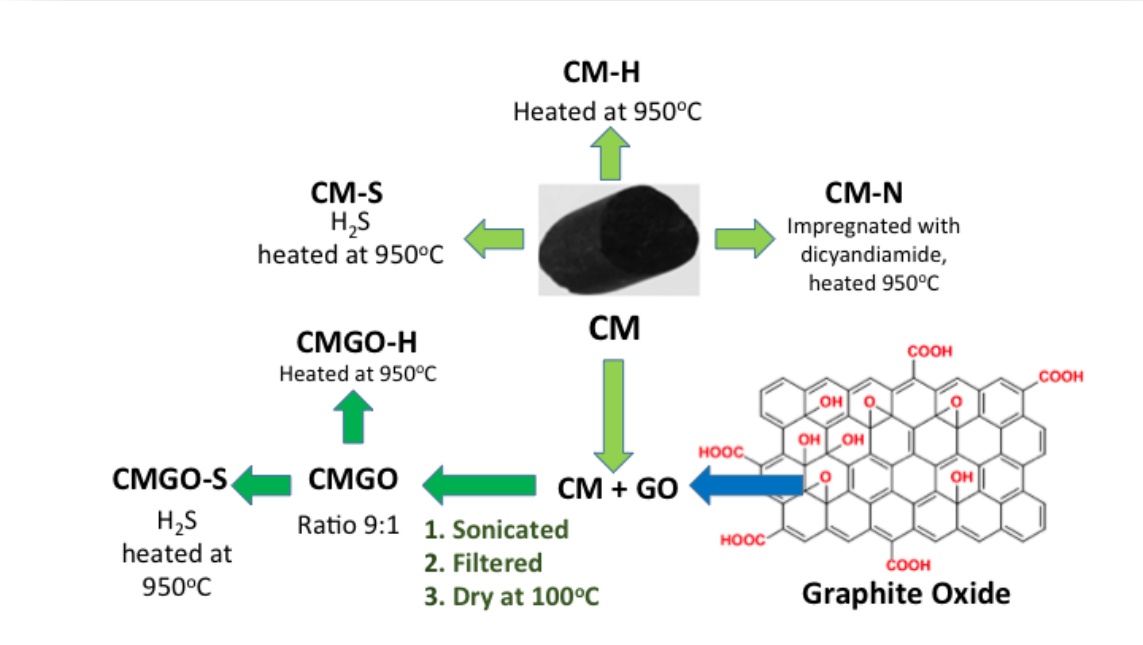

Figure 1: Schematic view of the samples' modification procedure.

2.2. Methods

2.2.1. Electrochemical Measurements. The CV (Cyclic Voltammetry) and LSV (Linear Sweep Voltammetry) of the as-prepared samples were analyzed by using a computer-controlled potentiostat (CHI 760C CH Instrument, USA). A typical three-electrode cell was used with platinum wire as the counter electrode, Ag/AgCl (1M KCl) as the reference electrode and a rotating ring-disk electrode (RRDE) as the working electrode in 0.1M KOH for the electrochemical measurements. The working electrodes were prepared by dispersing 5 mg of the as-prepared catalyst in 1 mL of deionized water and 0.5 mL of 1 wt. % Nafion® aqueous solution by sonication and drop casting 15 μL of the above dispersed solution onto the RRDE. The dried electrode was immersed into the 0.1M KOH solution which was saturated with N_2 gas for 1 hour, and the cyclic voltammograms (CV) curves were recorded for 10 times at a scan rate of 100 mV s^{-1} for stabilization of the catalysts. The potential was swept from 0.19 to -0.8 V vs. Ag/AgCl (1.17 V to 0.18 V vs. RHE). The CV curves were overlaid one over another to check if the electrode was stabilized and then two CV curves were recorded at a scan rate of 5 mV s^{-1} in the N_2-saturated 0.1 M KOH electrolyte. Next, the electrolyte was saturated with O_2 for 30 min and two CV curves were recorded at a scan rate of 5 mV s^{-1}. This step was repeated one more time and overlaid to see that there was no change in the onset and peak potentials. Finally, the Linear Sweep Voltammetry (LSV) measurements were carried out at different rotation speeds (400-2000 rpm) with continuous O_2 purging. The % peroxide generated (eq. 1) and the electron transfer number (eq. 2) were calculated from the LSV's using the following equations.[43]

$$\% HO_2^- = \frac{200 \times \frac{I_r}{N}}{I_d \times \frac{I_r}{N}} \quad (1)$$

$$n = \frac{4 \times I_d}{I_d + \frac{I_r}{N}} \quad (2)$$

where I_d and I_r are the ring and disk currents measured with RRDE. All the experiments were conducted at room temperature and the collection efficiency number N was determined to be 0.424 from the redox reaction of $K_3Fe(CN)_6$. The onset potential was chosen as the highest potential for the cathodic reactions at which a reaction product is formed at a given electrode. The corrections for capacitive current were applied in all data analyses.

To study the tolerance of the carbon catalysts to methanol, 0.2 mL of CH_3OH were added into the electrochemical cell. The final concentration of methanol (0.2 mL, three times) added to the electrochemical cell (40 mL, 0.10 M KOH) was 0.36 M. The working electrode was prepared by mixing the active material with polyvinylidene fluoride (PVDF) and commercial carbon black (acetylene black, 50 % compressed, Alfa Aesar) (8:1:1) in N-methyl-2-pyrrolidone.

The stability tests were done by running 1000 CV cycles in the potential range of -0.1 to -0.5 V vs. Ag/AgCl (0.88 V to 0.48 V vs. RHE) in an O_2-saturated electrolyte after the stabilization of the electrode in a nitrogen-saturated electrolyte in the potential range of 0.19 to -0.8 V vs. Ag/AgCl (1.17 V to 0.18 V vs. RHE). The currents at the maximum of ORR reduction hump were used to evaluate the catalyst stability.

The measured potentials versus the Ag/AgCl (1M KCl) reference electrode were converted to the reversible hydrogen electrode (RHE) scale using the Nernst equation[43]:

$$E_{RHE} = E_{Ag/AgCl} + 0.059pH + E^{o}_{Ag/AgCl} \quad (3)$$

where E_{RHE} is the converted potential versus RHE, $E_{Ag/AgCl}$ is the experimental potential measured against the Ag/AgCl reference electrode, and $E^{o}_{Ag/AgCl}$ is the standard potential of Ag/AgCl (1 M KCl) at 25°C (0.235 V). The electrochemical measurements were carried out in 0.10 M KOH (pH = 13) at room temperature; therefore, $E_{RHE} = E_{Ag/AgCl} + 1.002$ V.

The geometric surface area of the rotating ring-disk electrode is 0.126 cm^2 determined from geometrical measurement. Since the nanopores of the catalysts are accessible for oxygen molecules but possibly not for bigger molecules like $K_3Fe(CN)_6$, the effective surface areas can not be accurately measured by the generally used chronocoulometry of $K_3Fe(CN)_6$ method. Thus, the effective surface areas reported here are directly calculated from the weight of the catalyst loaded on the electrode and its BET surface area measured form adsorption of nitrogen. They are 320.0 cm^2, 298.0 cm^2, 314.0 cm^2, 327.5 cm^2, 196.5 cm^2, 251.5 cm^2 and 242.5 cm^2 for CM, CMGO, CM-H, CMGO-H, CM-N, CM-S and CMGO-S respectively.

2.2.2. Scanning Electron Microscopy (SEM). Scanning electron microscopy (SEM) images were obtained with a FEI Helios NanoLab 48 instrument. The accelerating voltage was 5.00 kV. The imaging was performed *in situ* on the powder samples, using a gold layer 5 nm thick.

2.2.3. Mercury porosimetry. Mercury porosimetry was carried out using an AutoPore IV 9500 device (Micrometrics, USA), according to two steps: (i) evacuation of the sample holder with the material inside and filling with mercury in a low-pressure chamber within the pressure range 0.001 – 0.24 MPa; (ii) transfer of the sample holder filled with sample and mercury to a high-pressure chamber and pressure increase from 0.24 to 414 MPa. The entrance diameters of pores in which mercury was forced to penetrate were estimated by application of Washburn's equation:

$$D = -\frac{4\gamma\cos\theta}{P} \quad (4)$$

where D (nm) is the intruded pore size, γ (485 mJ m^{-2}) is the surface tension of mercury, θ (140°) is the contact angle between the mercury and the material, and P (MPa) is the intrusion pressure.

2.2.4. Evaluation of Porosity. Sorption of nitrogen at -196°C was carried out using an ASAP 2020 (Micromeritics, Surface Area and Porosity Analyzer). Before the experiments, samples

were out-gassed at 250^{o}C to constant vacuum (2×10^{-6} Torr) for more than 48 h. Those temperature and long degassing time were chosen based on the results of thermal analysis indicating that no surface groups decompose at lower temperatures from these carbons. The BET surface area, total pore volumes, V_t, (from the last point of isotherm at relative pressure equal to 0.99), micropore volume, volume of pores narrower than 0.7 nm and 1 nm, $V_{<0.7nm}$ and $V_{<1nm}$, respectively, and mesopore volumes along with pore size distributions were calculated from the isotherms. The volume of mesopores, V_{meso}, represents the difference between total pore and micropore volumes. The volume of pores and pore size distribution were calculated using 2D-NLDFT approach assuming a heterogeneous surface of pore walls.[44]

2.2.5. Potentiometric Titration. Potentiometric titration (PT) measurements were performed with an 888 Titrando automatic titrator (Metrohm). Details of the experimental procedure are presented in the literature.[45] The experimental data were transformed into proton-binding curves, Q, representing the total amount of protonated sites. From them the pK_a distributions and the numbers of groups represented by certain pK_a values were calculated.[45,46]

2.2.6. X-Ray Photoelectron Spectroscopy (XPS). The XPS measurements were carried using a Physical Electronics PHI 5000 VersaProbe II spectrometer with a monochromatic Al Kα source (1486.6 eV) operating at 15 kV and 50 W, with 10^{-8} Pa vacuum in the analyser chamber. High-resolution spectra of powdered samples were recorded at a take-off angle of 45^{o} with a constant pass energy value of 29.35 eV, using a 200 μm diameter analysis area, whilst 117.4 eV pass energy was used for the survey spectra and used for the calculation of surface atomic concentration. The spectrometer energy scale was calibrated using Cu $2p_{3/2}$, Ag $3d_{5/2}$, and Au $4f_{7/2}$ photoelectron lines at 932.7, 368.3, and 84.0 eV, respectively. The SmartSoft-VP2.6.3.4 software package was used for acquisition and data analysis, and the Multipack software was

used to fit photoelectron spectra. A Shirley-type background was subtracted from the signals. Recorded spectra were always fitted using Gauss–Lorentz curves in order to determine the binding energy of the different element core levels more accurately.

2.2.7. Thermal analysis. Thermogravimetric (TG) curves were obtained using a TA instrument thermal analyzer (SDT Q 600), which was connected to a gas analysis system (OMNI Star^{TM}) mass spectrometer. The carbon sample was heated up to 1000^{o}C (10^{o}C min^{-1}) under a constant helium flow (100 mL min^{-1}). From the TG curves, differential TG (DTG) curves were derived.

2.2.8. Water Adsorption. Prior to water adsorption, the CM series of samples were dried at 120^{o}C for 12 hours and then cooled in a desiccator to room temperature. Afterwards, the predetermined amounts of dry samples were exposed to water vapors (30 mL of water in 1.1 L closed vessel) in air-tight environments for 24 hours at 22^{o}C. The amounts adsorbed were measured gravimetrically using a TA instrument thermal analyzer (SDT Q 600). The weight loss in nitrogen between 30 and 120^{o}C was assumed as an equivalent to the quantity of water adsorbed on the surface.

2.2.9. Metal content analysis. The metal content analysis (of the ashes) was done in Asbury Carbons using an ICP atomic adsorption spectrometer (Varian, Vista MPX ICP-OES). The sample was placed into a platinum crucible, introduced into a furnace at a low temperature, and then burnt at 700^{o}C. Approximately one gram of lithium tetraborate flux was added to the ash and held at 950^{o}C until the ash constituents were dissolved in the flux. The resultant materials were next dissolved in a hydrochloric acid solution, which was diluted to 200 mL for analysis by ICP-OES. The instrument is calibrated with each use, using a series of aqueous standards, which are matrix-matched as closely as possible to the unknown samples.

3. RESULTS AND DISCUSSION

3.1. Materials' characterization

A particular porosity in the range of micro and macropores of the carbon meringues was a feature, which directed us to choose a representative of these groups of porous carbons for further study of ORR efficiency upon various surface modifications. Even though these materials were described in details in Ref. [40], Figures 2(a)-2(c) collect SEM images of CM whereas Figures 2(d)-2(e) show mercury porosimetry data. It can be seen that the material has the typical structure of a carbon foam, with a rather broad distribution of cell sizes roughly ranging from 300 to 600 µm (see Fig. 2(a) and Ref. [40] for more details), but with a much narrower distribution of window sizes centered on *ca*. 100 µm (see Fig. 2(a) and 2(e)). The bulk density of the material was 0.043 g cm^{-3}, corresponding to a total porosity of 97.8%. Besides, the porosity is truly hierarchical, since higher magnification reveals two additional populations of pores having typical diameters of 10 µm on one hand, and below 1 µm on the other hand (see Fig. 2(b) and 2(e)). At the highest magnification, the carbon of which the material is made is based on small nodules, thus resembling the structure of a carbon aerogel (see Fig. 2(c)). Such a feature accounts for the presence of microporosity, as the measured BET surface area was indeed higher than 600 m^2 g^{-1} (see below). All these characteristics were thus expected to favor the deep penetration of the inner porosity by GO flakes. As shown previously, this GO was indeed able to penetrate silica gel pores of much smaller diameters than those of carbon meringues.[11]

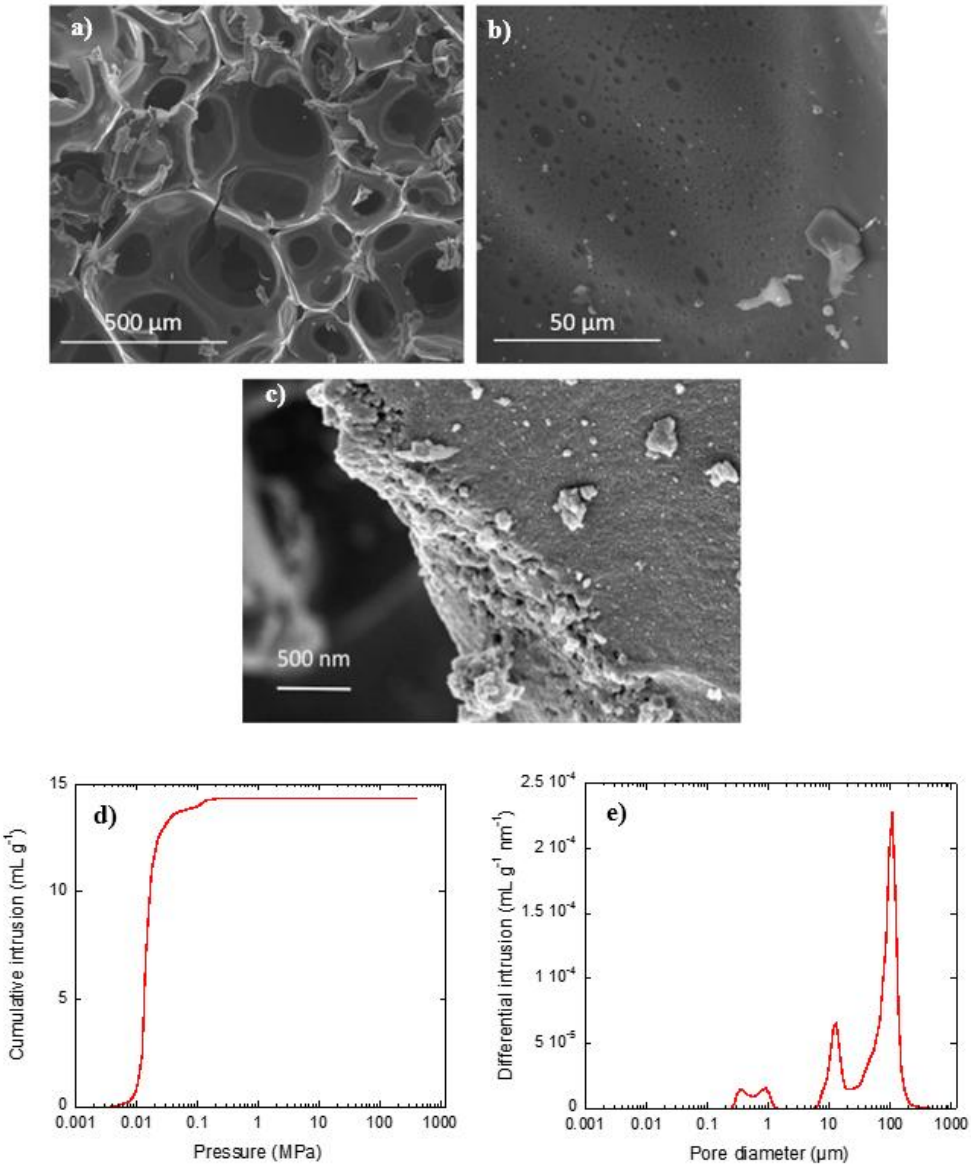

Figure 2. (a), (b) and (c) SEM images on the CM sample at different magnifications; (d) and (e) Cumulative and differential mercury intrusion curves, respectively.

Even though macroporosity is important for our modifications, chemical changes in smaller pores that might affect surface interactions either with oxygen or electrolyte are of paramount importance for our research goal. Thus, the nitrogen adsorption isotherms were measured (Figure 1S of Supplementary Information) and the parameters of pore structure and pore size

distributions, PSDs, were calculated from them and are presented in Table 1 and Figure 3, respectively. As seen, the addition of 10 wt. % GO (GMGO) decreased the surface area, the volume of micropores, and the total pore volume. Interestingly, a marked increase in the volume of mesopores was found. This indicates that GO was deposited in some macropores and its presence indeed decreased their sizes to the range of mesopores. It is important to recall that macropores cannot be detected from nitrogen adsorption studies. Since the shapes of the isotherms for all samples indicate a high degree of microporosity, these pores must exist in the carbon structure/macropore walls, as already suggested by the gel-like appearance seen in Fig. 2(c). Heating the CMGO composite (CMGO-H) further increased the volume of micro and mesopores. These possibly are the results of the reduction of GO phase. CO, CO_2 and water released in this process might act as activation agents. On the other hand, the heat treatment of CM left the porosity unaltered. High-temperature doping the CM surface with nitrogen or sulfur noticeably decreased the surface area, having a pronounced effect on the volume of very small micropores, especially in the case of nitrogen doping. This suggests that sulfur- and nitrogen-containing groups might be deposited at the entrances of these small pores and/or at the edges of distorted graphene layers where the most reactive surface sites are known to exist. Modification of the CMGO composite with hydrogen sulfide had a less pronounced effect on the decrease of surface area than that on CM. Interestingly, the decrease in the volume of ultramicropores for CMGO-S was more marked than that for CM-S (25 % decrease in CMGO-S versus 20 % for CM-S), which might be related to the reactivity of GO oxygen groups with hydrogen sulfide.

Table 1. The parameters of porous structure calculated from nitrogen adsorption measurements using 2D-NLDFT model (S_{BET} – BET surface area; V_t – total pore volumes; V_{meso} – volume of mesopores; $V_{<0.7nm}$ and $V_{<1nm}$ – volume of pores narrower than 0.7 nm and 1 nm, respectively, V_{mic} – micropore volume), and affinity of carbons towards water vapor (in wt. %).

Sample	S_{BET} ($m^2\ g^{-1}$)	V_t ($cm^3\ g^{-1}$)	V_{meso} ($cm^3\ g^{-1}$)	$V_{<0.7nm}$ ($cm^3\ g^{-1}$)	$V_{<1nm}$ ($cm^3\ g^{-1}$)	V_{mic} ($cm^3\ g^{-1}$)	V_{mic}/V_t	H_2O* (wt. %)
CM	640	0.324	0.018	0.251	0.279	0.306	0.94	3.65
CMGO	596	0.312	0.031	0.244	0.257	0.281	0.90	5.03
CM-N	393	0.211	0.026	0.135	0.157	0.185	0.88	2.13
CM-S	503	0.285	0.026	0.193	0.223	0.259	0.91	1.64
CM-H	628	0.320	0.025	0.234	0.263	0.295	0.92	1.97
CMGO-H	655	0.346	0.036	0.252	0.278	0.310	0.90	2.24
CMGO-S	485	0.287	0.06	0.149	0.193	0.227	0.79	2.26

*The amount of H_2O adsorbed by GO in the same conditions was 39.8 wt. %; GO is non-porous (S_{BET} = 6 $m^2\ g^{-1}$).

All the changes described above are seen in a comprehensive way on the PSDs presented in Figure 3. The changes are mainly seen in the volume of ultramicropores with an average diameter of ~0.6 nm which markedly decreased as a result of the applied modifications. Nevertheless, the size of pores remained unchanged. The only exception is CMGO-S, for which the size of ultramicropores increased to 0.7 nm, and larger micropores with diameters between 0.8-0.9 nm seen in other carbons were not detected in this material. These changes might affect the ORR process on CMGO-S.[37]

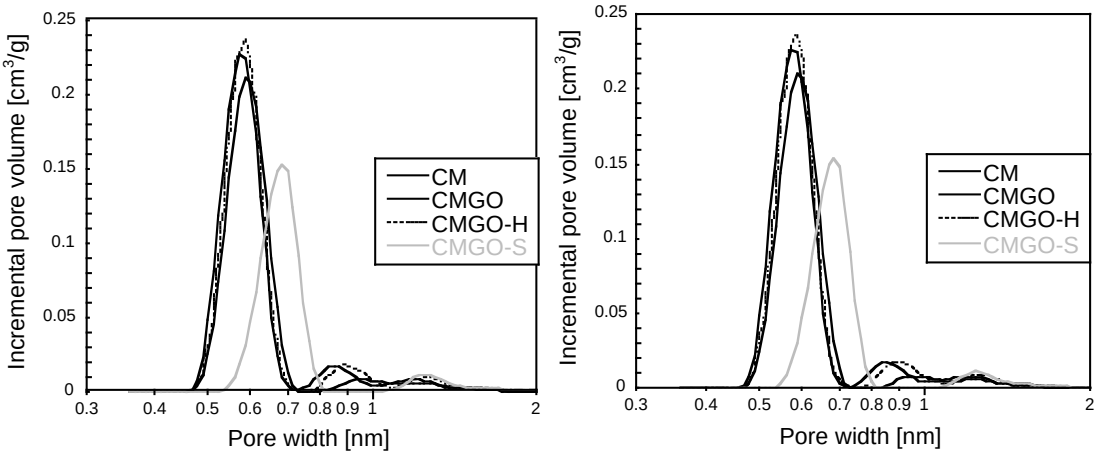

Figure 3. Pore size distributions for the carbons studied calculated using 2D-NLDFT.

Besides their effects on porosity, the modifications applied were expected to alter surface chemistry to an even greater extent. Potentiometric titration provides the information about the average surface pH, number of acidic groups on the surface, and the distributions of their pK_a values. The proton binding curves are presented in Figure 4 and the number of strong and weak acidic groups, and surface pH values are collected in Table 2. The details on the pK_a distributions are presented in Figure 2S and Table 1S of the Supplementary Information. All samples exhibit basic pH and show a proton uptake indicating the basic character of their surfaces. The least basic and exhibiting a very small extent of the proton release process is the composite with GO. This is due to the strongly acidic character of GO located inside the pores of this sample. The highest pH values and the smallest numbers of dissociating groups are on the surface of CM-H and on those of the sulfur-modified samples, CM-S and CMGO-S. Interestingly, nitrogen-modified sample is very rich in groups dissociating in our experimental pH window.

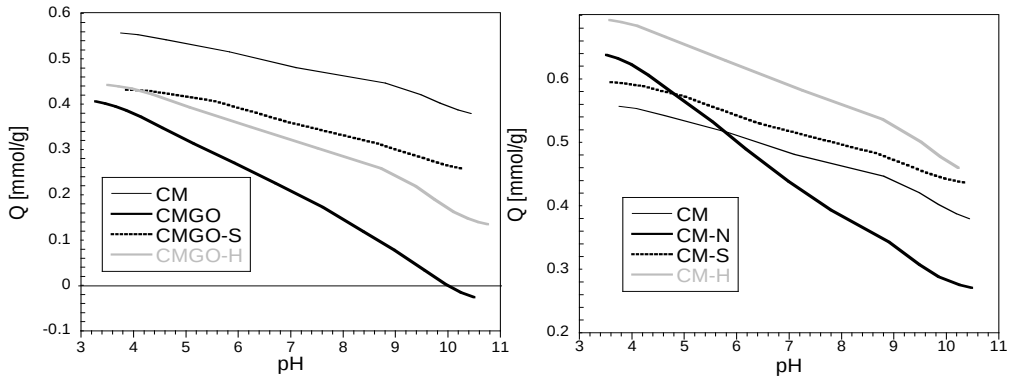

Figure 4. Proton-binding curves.

Table 2. Surface pH values, amounts of groups detected from potentiometric titration (in mmol g^{-1}), and content of elements on the surface detected by the XPS analysis (in at. %).

Titration					XPS			
Sample	pH	$pK_a<7$	$pK_a>7$	Total number of groups	C	O	N	S
CM	8.83	0.103	0.092	0.195	86.4	13.6	Nd	nd
CMGO	7.90	0.243	0.210	0.453	80.7	19.3	Nd	nd
CM-H	9.07	0.102	0.063	0.165	83.4	14.3	2.3	nd
CMGO-H	8.60	0.115	0.208	0.323	89.6	10.0	3.4	nd
CM-N	8.56	0.197	0.186	0.383	75.6	20.7	3.7	nd
CM-S	9.90	0.102	0.063	0.165	90.7	8.10	Nd	<1
CMGO-S	9.29	0.042	0.143	0.185	85.9	14.1	<1	1.2

nd-not detected

To further investigate the differences in surface chemistry, TG analysis in helium was carried out and the differential (DTG) curves are collected in Figure 5. The TG curves are included in Figure 3S of the Supplementary Information. On DTG curves, the peaks represent the weight losses related to the decomposition of surface groups, and the area under them are directly proportional

to the weight loss/amount of decomposing groups. A peak at about 100^{o}C represents the desorption of physically adsorbed water. For CM, carboxylic groups decompose between 200 and 400^{o}C, followed by the decomposition of anhydrides and lactones at about 600^{o}C.[47, 48] At temperature higher than 700^{o}C, phenols, ethers and carbonyls structures decompose. On the other hand, the addition of GO results in the appearance of a sharp peak at 200^{o}C representing the decomposition of epoxy groups of GO. Its OH groups decompose at temperatures higher than 800^{o}C. Heating both CM and CMGO at 950^{o}C evidently "cleans" their surfaces from surface groups, which is consistent with the potentiometric titration results. While nitrogen-doped sample shows gradual weight loss mainly between 100 and 400^{o}C and over 800^{o}C, sulfur-modified carbons show markedly different patterns. On the DTG curve for CMGO-S, a very small weight loss between 400 and 600^{o}C is revealed. This is followed by an increasing weight loss at temperature higher than 700^{o}C. The DTG curve for CM-S, besides weight losses in the same range of temperature as those for the composite, reveals intense peaks at 700 and 800^{o}C. This indicates differences in sulfur chemistry between these two sulfur-doped samples. The composite is apparently chemically more homogeneous. The weight loss between 400 and 600^{o}C can be linked to the decomposition of sulfoxides/sulfones bonds, and those at temperature higher than 750^{o}C to the decomposition of sulfur in sulfides and thiophenic configurations.[49] Small intensities of the peaks representing losses of physically adsorbed water suggest the high hydrophobicity of the sulfur-doped samples.

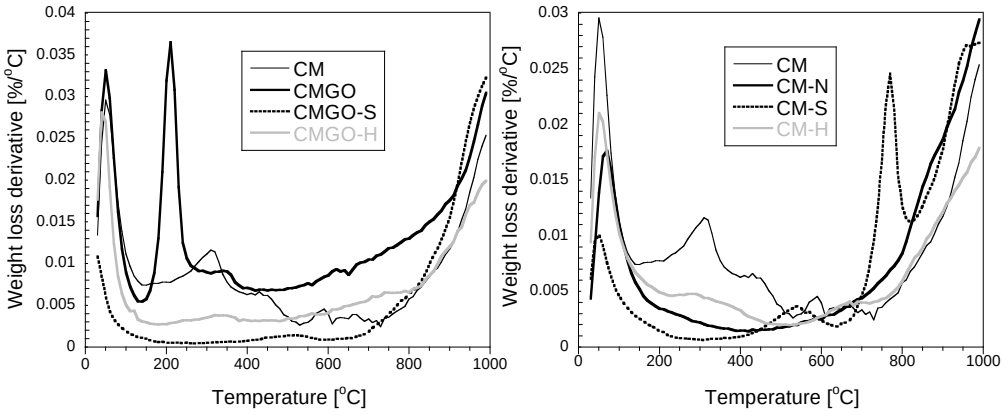

Figure 5. DTG curves in air for the samples tested.

The view of surface chemistry derived from the potentiometric (PT) and thermogravimetric (TG) analyses is supported by the XPS analysis. The atomic content of elements on the surface is presented in Table 2. Interestingly, nitrogen was detected not only on the surface of CM-N but also on the heat-treated CM and CM-H. Its presence is related to the use of hexamine as crosslinker in the synthesis procedure. It forms complexes with tannin that are incorporated in the thermoset polymer structure,[40] and some of these nitrogenated moieties are the residue of this process. Lack of detected nitrogen on CM and CMGO can be linked to screening effect of oxygen groups on the surface. Upon their decomposition and removal of carbon atoms as a result of heat treatment, as suggested by the TG and PT data, nitrogen groups are exposed and detected by XPS on these samples. On the surface of the H_2S-treated samples, nitrogen was also not detected and on CM-S and CMGO-S only less than 1 at. % and 1.2 at. % sulfur was found, respectively. These two samples have also the smallest contents of oxygen. While on CMGO-H, as expected, heat treatment decreased almost twice the content of oxygen mainly due to the reduction of GO, the content of oxygen on the surface of CM and CM-H being basically the same after such treatment. Even though this is consistent with the PT results, the TG analysis showed the marked difference in weight loss between these two samples. A plausible explanation

is a difference in the principles of the methods. While both XPS and PT are surface techniques, TG is a bulk analysis, where the content of the carbon matrix is also included. A very high content of oxygen in CM-N is consistent with the potentiometric titration results.

Table 3. The results of deconvolution of C 1*s*, O 1*s*, S 2*p* and N 1*s* core energy levels.

Energy, eV	Bond assignment	CM	CM-H	CM GO	CM GO-H	CM-N	CM-S	CM GO-S
C 1*s*								
284.8	C-(C, S) (graphitic carbon)	73.0	66.9	62.7	78.7	77.9	80.1	78.9
286.3	C-(O, N, S, H) (phenolic, alcoholic, etheric)	14.9	19.4	17.5	12.1	13.1	12.5	12.4
287.1	C=O (carbonyl or quinone)	8.0	9.4	14.6	5.1	5.4	4.9	5.0
288.6	O-C=O (carboxyl or ester)	2.2	2.1	3.1	2.4	3.4.	1.7	2.1
290.0	π–π^*	1.8	2.2	2.1	1.6	1.2	0.8	1.6
O 1*s*								
531.5	O=C/O=S (in carbonyl/ quinone or sulfoxides/ sulfones)	7.3	5.2	9.7	9.0	5.6	8.9	3.2
533.0	O-C/O-S (in phenol/epoxy or thioethers/sulfonic)	82.6	80.9	71.9	85.7	90.9	71.9	86.1
534.35	-O- (in carboxyl, water or chemisorbed oxygen species)	10.1	13.9	18.3	5.3	3.4	18.3	10.6
N 1*s*								
398.5	N-6 (in pyridine)		46.1		46.3	47.8		
400.5	N-5 (in pyrrolic/pyridone and azo nitrogen)		53.9		53.7	33.3		
402.4	N-X (in pyridine-N-oxide)					18.9		
S 2*p*$_{3/2}$								
164.0	R-S-S-, C-S-C (in bisulfides / thiophenes configurations)						83.0	100.
167.3	R_2-S=O/R-SO_2-R (in sulfoxides, sulfones)						17.0	

More details on the surface chemistry are provided by the deconvolution of the C1*s*, O1*s*, N1*s* and S2*p* core energy levels[24,29] (see Table 3 and Figure 4S of the Supplementary Information). Analysis of the contributions of C1*s* did not show very big differences between the samples. The only noticeable difference was in the case of the noticeable contribution at 286.3 eV for CM-H compared to that for CM. This contribution, besides phenolic groups, can be related to the nitrogen in C-N bonds. The CMGO sample has the marked contributions of carbon in C-O and C=O bonds related to the presence of GO. These groups were reduced after heat treatment and the contribution of C-C bonds in sp^2 configuration significantly increased. Sulfur-doped samples and CMGO-H have the smallest contributions at high binding energies on C1*s* spectra, indicating the lowest level of oxidation. This is consistent with a low content of oxygen on their surfaces and with the smallest amounts of acidic groups detected using potentiometric titration.

The deconvolution of O1*s* core energy level spectra showed three contributions for all samples: oxygen in carbonyl/quinones and sulfoxides/sulfones at 531.3 eV, phenol, epoxy, and thioester/sulfonic groups at 533 eV, and carboxyl, water or chemisorbed oxygen species at 543.3 eV. The contribution at 531.3 eV was the smallest for CNGO-S, but the highest for CMGO. On the other hand, the latter sample had the smallest contribution at 533 eV (phenol, epoxy) but the highest one of carboxylic acid /chemisorbed oxygen. Heating at 950^{o}C significantly decreased that contribution. No significant change was found for the distribution of oxygen species for CM-H. Interestingly, for CM-N the contribution of oxygen in phenol and epoxy groups is the highest. For this sample, and although the signal is noisy owing to the low sensitivity of the instrument used, the deconvolution of N1*s* indicates the presence of species at binding energy of 402.4 eV linked to pyridinic N-oxide. This can explain the high content of oxygen in this sample. On the surface of CM-H and CMGO-H, nitrogen is present only as pyridine and pyrolic/azo

nitrogen. As indicated above, this nitrogen originates from the nature of the crosslinker (hexamine: $C_6H_{12}N_4$) used for preparing the carbon foams.

The deconvolution of S2*p* core energy levels shows that in CMGO-H sulfur is present only in a reduced form as bisulfide and thiophenes, and in CN-S there is a small contribution of sulfoxides at 167.3 eV. This chemical heterogeneity was also seen in the TG curves and was discussed above (Figure 5).

To ensure that the materials tested do not contain transition metals such as iron, known as an ORR catalyst, the ash composition of the parent CM sample was analyzed. The detailed results are presented in Table 2S of the Supplementary Information. The main components of ash are K, Mg and Ca whose contents in the original sample are 8196, 3044, and 2757 ppm. The content of iron is only 1 ppm and it is four orders of magnitude smaller than in the work of Dai and coworkers, who found 1.1 wt % in their carbon-based purified catalyst [39]. On the purified sample with only 0.11% of iron, their ORR activity significantly decreased. Therefore, no marked catalytic effect on the catalytic performance of our carbons is to be expected.

The water uptake is directly linked to surface chemistry affecting polarity/hydrophilicity level (Table 1). Even though the porosity can play some role, generally it is accepted that when less water is adsorbed, the more hydrophobic is the surface. Heating at 950^{o}C decreases the affinity of the surface towards water owing to the decomposition of oxygen-containing groups. The most hydrophobic foams are CM-H and CM-S. CMGO-H and CMGO-S have similar level of hydrophobicity. Some affinity of the latter sample to adsorb water can be related to its higher volume of mesopores. In fact, functional groups containing oxygen can only exist in the pores larger than 1 nm (supermicropores and mesopores) and they are mainly responsible for attracting water. They are also expected to attract an aqueous electrolyte with dissolved oxygen; however,

based on their volume, the highest amount of oxygen is expected to be adsorbed in the pores of CM and CMGO-H and the smallest one in CM-N and CMGO-S, provided that the electrolyte has the same access to the entrance of the pores smaller than 0.7 nm. Obviously, the situation is more complex and surface chemistry is expected to affect that access. The distribution of catalytic centers is also expected to play an important role.

3.2. Electrochemical performance in alkaline solution

The cyclic voltammograms (CV) curves measured in the 0.1 M KOH electrolyte saturated either with O_2 or N_2 are presented in Figure 6. In each case the geometrical surface of the electrode was kept the same. The CV curves for the Pt/C were reported previously.[37] The maximum of ORR hump for this sample is at 0.85 V vs. RHE. The most pronounced humps related to oxygen reduction are seen for CM-S, GM-H and CMGO-H. These samples also happened to be the most hydrophobic, as listed in Table 1. Even though a smaller amount of water was adsorbed on CM-N than on CMGO-H, this trend can be linked to the almost twice smaller surface area of the former sample.

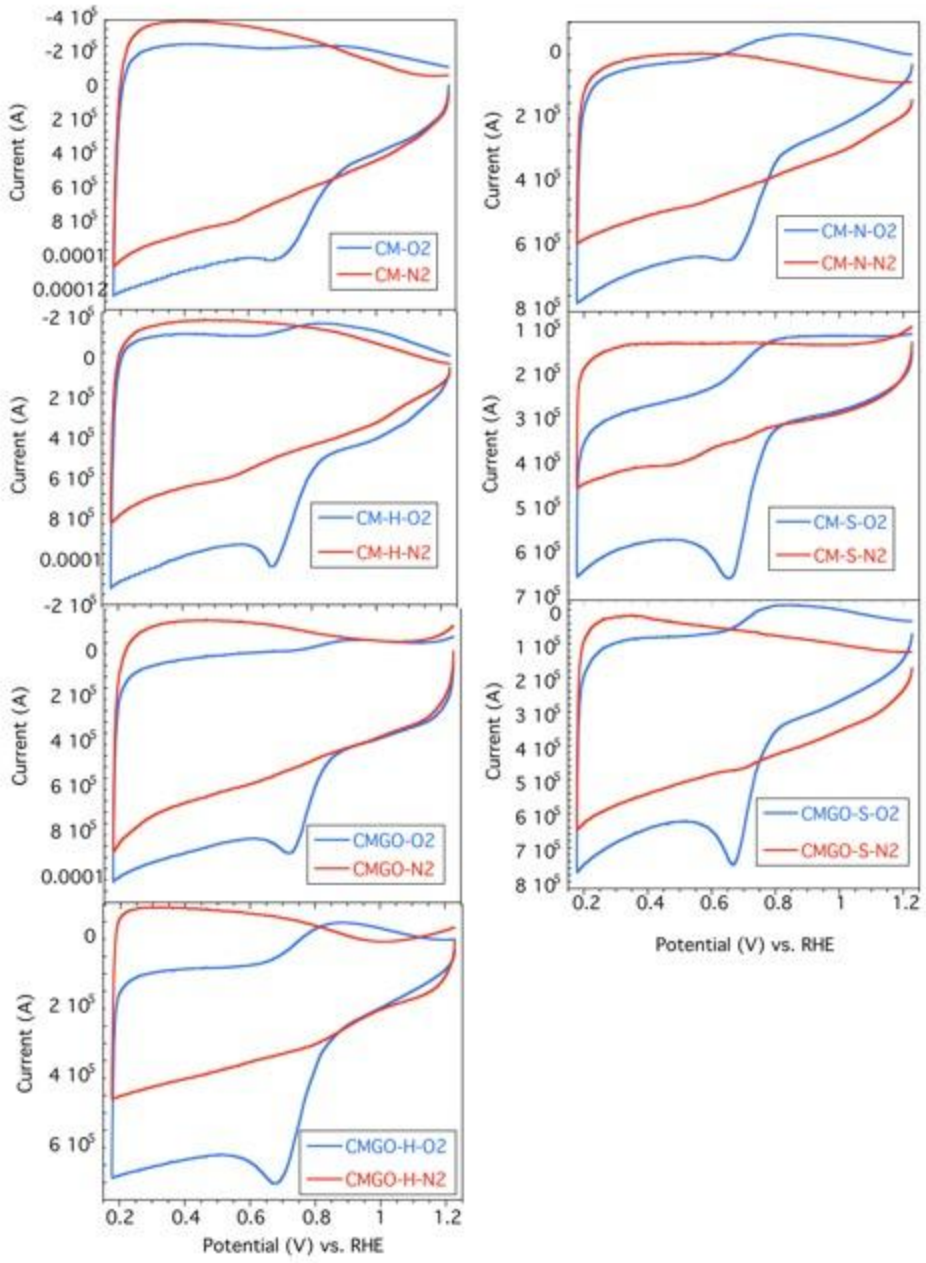

Figure 6. Cyclic voltammograms measured using RRDE in 0.10 M KOH at scan rate of 5 mV s^{-1} for the materials studied.

The onset potentials, defined as the highest potentials at which the ORR reaction starts, are compared in Figure 7A. The comparative plot of the LSV results at the rotation speed 2000 rpm is presented in Figure 7S of the Supplementary Information. CM sample exhibited the most positive onset potential. Addition of GO made it less positive. Heating both CM and CMGO at 950^{o}C also made the onset potential less positive. Interestingly, the extent of that decrease effect on the onset potential for CMGO-H is much smaller than that for CM-H. As it was proposed previously,[37] the observed effect of these modifications on the onset potential can be directly linked to some changes in the porosity and in the degree of hydrophilicity. Obviously, the addition of GO resulted in much more hydrophilic surface than that of CM. The porosity in the range of small pores decreased and this resulted in less affinity of the surface to withdraw oxygen from electrolyte for its adsorption in small pores, promoting the reduction reaction. Heating CMGO at 950^{o}C markedly decreased its oxygen content and also made the surface much more hydrophobic as seen from the deconvolution of C1*s* and O1*s*. Its porosity became comparable to that of CM. Nevertheless, water showed more affinity to adsorb on CMGO-H than on CM, which is also seen in the higher number of groups dissociating in our pH window (Table 2 and Table 1S of the Supplementary Information). This results in the less positive onset potential on CMGO-H than that on CM. The heat treatment of CM, interestingly, introduced increased contribution of carboxylic groups (from O1*s* deconvolution) and decreased the volume of pores smaller than 0.7 nm, and these changes have a negative effect on the onset potential.

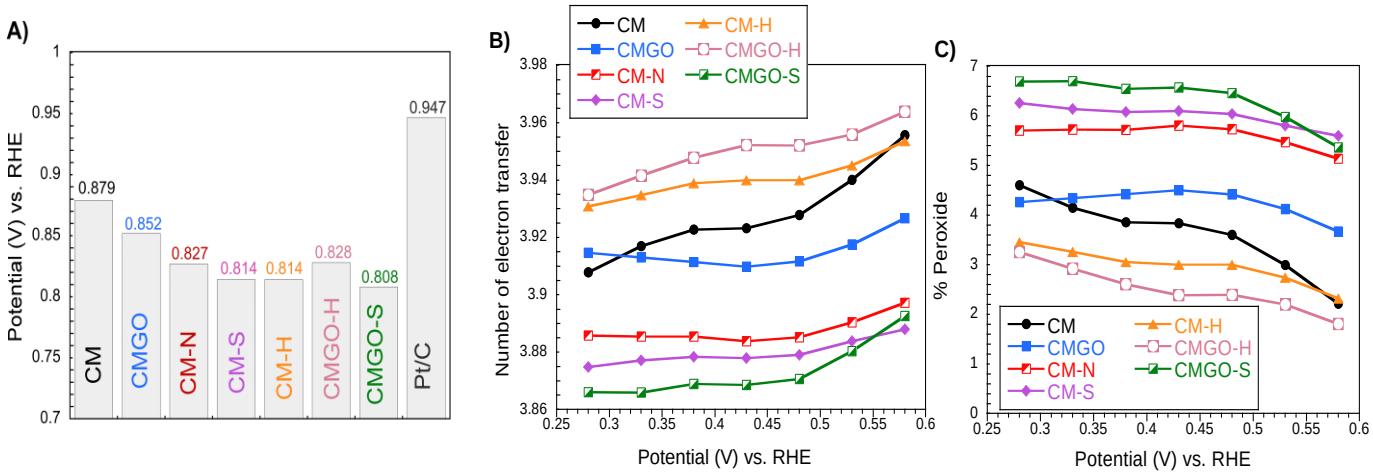

Figure 7. Comparison of the onset potential (A), number of electron transfer (B) and the percentage of oxygen reduced to peroxide. (C).

In the case of heteroatom-doped samples, besides the effects of hydrophobicity and porosity, the catalytic influence of nitrogen- and sulfur-containing groups is of paramount importance. Among these samples, the nitrogen-treated one showed the most positive onset potential and the behavior of the two S-containing samples were very similar with slightly better performance of CM-S. All these samples have a lower volume of narrow pores (< 0.7 nm) than CM and the CMGO series. In fact, CM-N shows the smallest volume of these pores, which are effective in promoting the adsorption of oxygen. Interestingly, this sample has the highest content of oxygen and groups dissociating in our pH window. This suggests that the reduction of oxygen must be predominantly the effect of catalytic sites associated to nitrogen[10] and not that of porosity. Even though the catalytic effect related to sulfur sites should also dominate the oxygen reduction on CM-S and CMGO-S, the higher hydrophobicity, the lower oxygen content and the higher surface

area of the CM-S surface might slightly enhance its performance compared to that CMGO-S, owing to the contribution of the pore effect to oxygen reduction mechanism in this case. Recent studies on the positive effects of porosity on the ORR activity indicate that a high volume of pores is important for the high dispersion of metal–free catalytic centers that enhance ORR.[33, 36, 50]

The oxygen reduction can occur via four electron pathways where O_2 is directly reduced to water, or the two electron pathways where O_2 is reduced to peroxide and consequently to water. The two-electron process is detrimental in fuel cells as the peroxide leads to corrosion of the cell components, eventually leading to the decrease in the fuel cell efficiency. From the results collected, the number of electron transfer and the % peroxide were calculated and are presented in Figure 7B and 7C, respectively. As expected, there is a reverse relationship between the amount of hydrogen peroxide detected and the number of electron transfer with respect to the potential (Figure 7C). Even though the number of electron transfer for all samples tested is close to 4, small differences exist. Thus, CMGO-H has the highest number of electron transfer between 3.96-3.93 in the potential range of 0.58 to 0.28V (vs. RHE) and the smallest peroxide yield (1.81-3.25%), indicating a predominant reduction of oxygen to water. The order in decreasing *n* value is as follows: CMGO-H > CM-H > CM > CMGO > CM-N > CM-S = CMGO-S. The opposite trend was found in hydrogen peroxide concentration. The highest numbers of electron transfer were found for the series of CM and CM-GO, and the smallest for the heteroatom-doped samples, which might be related to the differences in the mechanism indicated above. Nevertheless, as for the onset potential, the CM-N sample outperformed those doped with sulfur. On the latter, once again no marked differences in the *n* value were found.

To study the influence of the electron transfer kinetics on ORR on the vitreous carbon foams, the RRDE experiments were conducted in 0.1 M KOH solution at different rotation speeds from 400-2000 rpm (Figure 5S and 6S of Supplementary Information). The current density increased with the increased rotation speed due to the enhanced diffusion of the electrolytes and O_2. The Koutecky-Levich (K-L) plot was used to analyze the kinetic parameters such as kinetic current density (J_K) and the effective diffusion coefficient of O_2 (D_0). The equation to calculate the K-L plot is as follows[43]:

$$1/J = 1/J_L + 1/J_K = 1/(B\omega^{0.5}) + 1/J_K \quad (5)$$

where J is the measured current density, J_L and J_K are the diffusion limiting and kinetic limiting current densities, ω is the rotation rate of the electrode, and B is the Levich constant. B can be calculated using the equation $B = 0.62nFC_0(D_0)^{2/3}\nu^{-1/6}$ and $J_K = nFkC_0$, where n is the number of electron transfer in the ORR, F is the Faraday constant (F = 96485 C mol^{-1}), D_0 is the effective diffusion coefficient of O_2 (cm^2 s^{-1}), ν is the kinematic viscosity of the electrolyte (cm^2 s^{-1}), C_0 is the oxygen concentration (mol cm^{-3}) and k is the electron transfer rate constant. The K-L plot for the as-prepared samples at an electrode potential of 0.58V (vs. RHE) exhibited linearity at the low rotation speed regime (Figure 7S) where the linear fitting was performed.[51-52]

The slope and intercept of the linear part of the K-L plot give the Levich constant (B) and J_K, which are used to calculate the effective diffusion coefficient constant of O_2 (D_0) (Figure 7S) and the kinetic rate constant k. The doped samples CM-N, CMGO-S and CM-S have the highest kinetic rate constant, indicating the intrinsic good performance of the heteroatom doped samples. For the non heteroatom-doped samples, the kinetic rate constant and the effective diffusion coefficient exhibit the same trend as the ratio of the V_{mic}/V_t , suggesting that when catalytic dopants are not present, the micropore volume advances the oxygen diffusion and the reduction

reaction. In fact, CM has also the highest surface area. The order in the accessibility of the pores to oxygen is the following: CM > CM-H > CMGO > CMGO-H for the non-doped samples, and CM-N > CMGO-S > CM-S, for the doped ones. That order more or less follows the order of the surface area and some discrepancies are, for instance, the diffusion of oxygen on CM-N is better than that in CM-S, even though the surface area of the latter is markedly higher. This suggests that the diffusion of oxygen is influenced by the number of oxygen groups. More oxygen on the surface of CM-N promotes a higher degree of wettability of the pore system and thus the electrolyte with dissolved oxygen can get closer to the hydrophobic pores/catalytic centers.

The kinetic currents and kinetic current densities for each catalysts are compared in Figure 8A. In terms of absolute value of the kinetic current, the CM and CMGO series of samples outperformed heteroatom-modified carbon foams. The latter one has kinetic current densities about 30 % smaller than that of CM, which is an outstanding sample among those tested. CM-N and sulfur-doped samples behave quite similar at the least positive potential and then, with an increase in the potential, the advantage of CMGO-S over CM-N and CM-S is better visible.

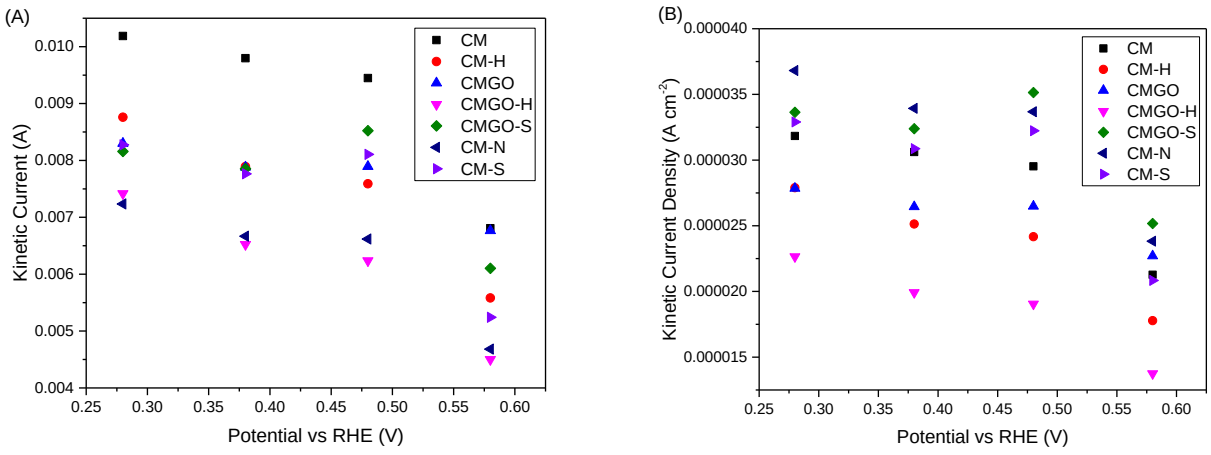

Figure 8. Kinetic current (A) and kinetic current density (B).

Since in our discussion we stressed the role of small pores combined with hydrophobicity in the process of oxygen reduction, the current densities calculated from the surface area based on BET measurements are compared in Figure 8B. While for the CM and CM-GO series, the order of the results did not change and still the differences related to surface chemistry can be seen, the heteroatom-doped samples presented a different picture of the catalytic activity. Now CM-N and CMGO-S are the best performing sample followed by CM and CMGO. This confirms the different mechanism and the effects of catalytic center of the heteroatom containing samples on ORR. Interestingly, even though some nitrogen was detected on the surface of CM-H and CMGO-H (Table 3) but the kinetic current density is the lowest. That nitrogen does not affect ORR to the same extent as that in CM-N. The only difference between the nitrogen-containing samples is that CM-N has nitrogen in pyridine N-oxides. They have the positive charge on nitrogen and the results suggest that these species can have a catalytic effect on ORR.

All carbons tested show a very high tolerance to methanol crossover at the potential of the maximum current of ORR (Figure 9). Indeed, injecting 0.2 mL of methanol three subsequent times (indicated as arrows in Figure 9) did not affect the current density in the case of the catalysts tested. On the other hand, when Pt/C was tested in the same conditions, a significant decrease in the current was noticed for each addition of methanol to the electrolyte, indicating the decrease in the activity of catalytic Pt-based centers.

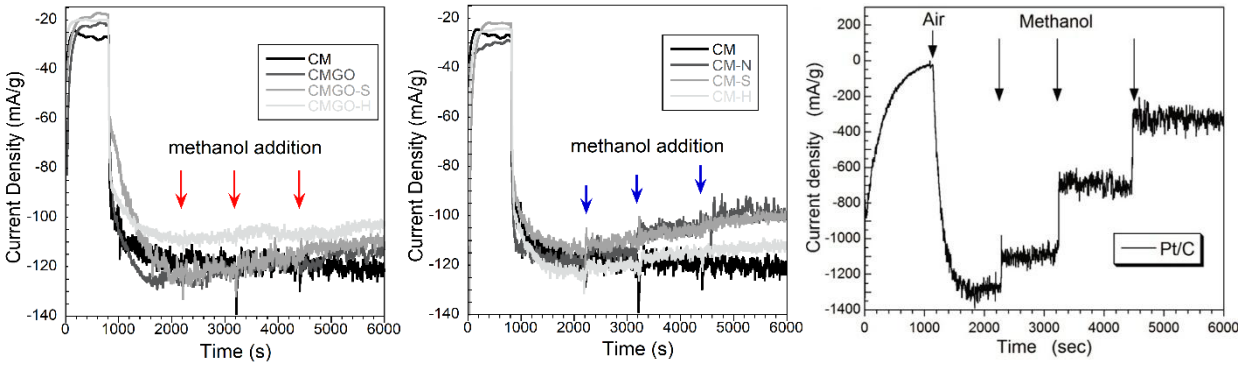

Figure 9. Chronoamperometry response for methanol crossover at the potential of the maximum of the oxygen reduction humps (results of methanol crossover test on Pt/C are reprinted with permission from Ref [37]. (Copyright 2016, American Chemical Society).

Stability tests were run arbitrarily to 1000 potential cycles (Figure 10). The best stability, and better than that of Pt/C, was found for CM-H whose performance after 1000 cycles remained at the 80 % level. The stability of Pt/C decreased to about 70% and it is very similar to that of the parent CM sample and CMGO. Interestingly for CM-S after the initial 30 % decrease in the performance in 400 cycles, the current density gradually increased and reached a plateau at the same level as for CM-H. This might be related to instability of sulfur compounds in this sample, which are likely oxidized by H_2O_2 formed *in situ*. The worst performance from the point of view of stability is presented by heteroatom-doped CM-N and CMGO-S. The current significantly drops at the beginning of the cycling tests and after 1000 cycles it remains on about 60 % of the initial performance. One of the factors affecting the stability is the speciation of the oxygen reduction products. If a marked quantity of H_2O_2 is formed (Figure 7), the oxidation of carbon surface is expected. Indeed, the highest amounts of hydrogen peroxide were formed in the case

of GMGO-S, CM-S and CM-N. Thus, oxidation of the surface resulting in either removal / change of active centers or changes in the porosity can be responsible the loss of catalytic performance. As expected, the effect is the strongest on the first exposure to oxidizing agent. An increase in the activity of CM-S after certain number of cycles is likely caused by oxidation and removal of sulfur species, which might result in in the similar surface to that of CM-H. These two samples were treated at 950^{o}C either in nitrogen or hydrogen sulfide.

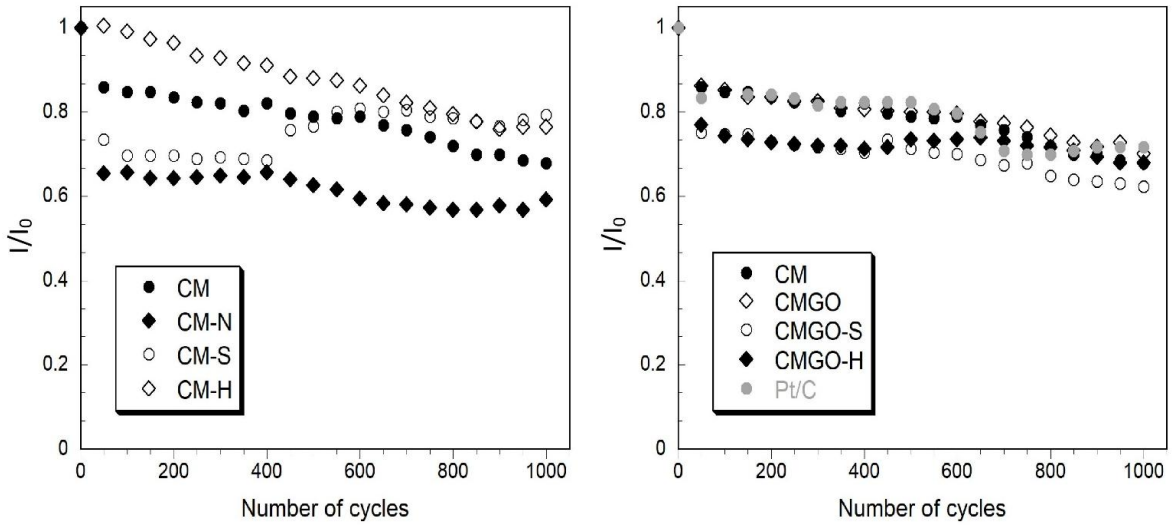

Figure 10. Stability of CM, CM-N, CM-S, CM-H, CMGO, CMGO-S, CMGO-H, and Pt/C in the ORR process over 1000 CV cycles.

Even though the analysis of the results collected indicates the marked role of small pores with a hydrophobic surface as catalytic sites for ORR, which advance the reduction by a different mechanism than that on heteroatom-containing sites, these findings are not contradictory to those published in the literature indicating the role of defect in the carbon matrix in ORR reduction [38, 39] In fact, a more developed surface obviously leads to more defects in the carbon matrix, which were indicated by Hu and coworkers[38] and Dai and coworkers[39] as the ORR reduction sites.

Moreover, our modification with GO was in line with findings by Dai and coworkers. They suggested that graphene oxide fragments formed by oxidation of their CNT increased the ORR activity, and in our case, the addition of GO to CM indeed increased the performance in terms of onset potentials. The treatment of CMGO at 950^{o}C might create more active defects enhancing the catalytic activity and the number of electron transfer.

Another support for our findings on the specific and important role of porosity is the recent results published on 3D interconnected carbon networks.[50, 53--53] Even though some of those structures contained nitrogen, and Fe or Co, the interconnect network architectures were indicated as promoting ORR by facilitating electron transfer and providing a high dispersion of active sites.

4. CONCLUSIONS

The results presented in this paper emphasize the role of small pores and their surface hydrophobicity in ORR on carbonaceous materials. We proposed and explored a new mechanism of O_2 reduction which is based on a different principle than the generally accepted mechanism of ORR reduction on heteroatom-doped carbons. Even though some carbon foams investigated here do not have "classical" catalytic centers for ORR, based on nitrogen and sulfur incorporated to the carbon matrix, they show a promising onset potential, a number of electrons transfer close to 4, and a relatively good kinetic current density. Such performance is linked to the specific porosity where small micropores and mesopores co-exist. The macropores promote the wettability of the surface with electrolyte, whereas micropores present in thick foam walls are the sites where oxygen reduction takes place. Owing to hydrophobicity of the ultramicropores (smaller than 0.7 nm), water does not have a tendency to enter them. At their entrances, oxygen,

which adsorbs on hydrophobic surfaces, moves from the aqueous phase to these pores where it is strongly adsorbed owing to the overlapping adsorption potential. Then the reduction process takes place and that oxygen is reduced mainly to water. The formed water rather does not stay in hydrophobic pores but is strongly attracted to larger pores. When this happens, the pores-oxygen reduction sites can efficiently adsorb/withdraw other O_2 molecules from the electrolyte. For this process the number of small pores is important. Even though we are not aware of the methods which could be used to calculate the number of pores in amorphous carbons, the differences in the volume of pores smaller than 0.7 nm between samples can be considered as an indication of such pore number. Even though the hydrophobicity in these pores and their sizes are crucial, some level of polarity in larger pores is beneficial to transport oxygen dissolved in the electrolyte to these small pores' entrances.

On the other hand, the modification of the carbon surface with heteroatoms applied in this work decreased the porosity as well as introduced the heteroatom dopant-based catalytic centers promoting ORR. This dramatically changed the mechanism of ORR. Still the number of electron transfer was close to 4 but with a less positive onset potential. We also noticed that even though the current density can be increased due to the introduction of more active centers, catalytic centers from these heteroatom dopants are nevertheless not stable upon generation of oxidative species, such as H_2O_2 during ORR process.

The results obtained suggest that non-doped carbons can be used as efficient ORR catalysts. Such materials can be a more cost-effective alternative to Pt/C than heteroatom-doped graphene. Tuning porosity and surface chemistry of porous carbons is crucial to fully use the promise that the small pores provide for ORR. This new mechanism we propose is based on the affinity of oxygen to strongly adsorb in small hydrophobic pores. The results presented offer an

alternative/complementary route to explain the ORR activity of porous carbon-based catalysts addressed recently in the literature.

AUTHOR INFORMATION

Corresponding Author

*E-mail: tbandosz@ccny.cuny.edu.

Notes

The authors declare no competing financial interest.

SUPPORTING INFORMATION.

Nitrogen adsorption isotherms, TG curves, pK_a distributions, deconvolutions of core energy level spectra, linear sweep voltammograms, K-L plots, and the results of ICP analysis. This material is available free of charge via the Internet at http://pubs.acs.org.

ACKNOWLEDGMENT

The French group gratefully acknowledges the financial support of the CPER 2007-2013 “Structuring the Competitiveness Fibre Cluster”, through local (Conseil Général des Vosges), regional (Région Lorraine), national (DRRT and FNADT) and European (FEDER) funds. The HE group acknowledges the financial support provided by the National Science Foundation (CBET 1438493 and DMR 1507812). The authors are grateful to Dr. Mykola Seredych for his experimental involvement in sample modifications and in collecting some surface characterization data and to Dr. Dimitrios Giannakoudakis for collecting SEM images of a high

magnification. Mr. Albert V. Tamashausky from Asbury Carbons is thanked for providing ICP analysis data.

REFERENCES

(1) Steele, B. C. H.; Heinzel, A. *Nature* **2001**, *414*, 345-352.

(2) Armand, M.; Tarascon, J. M. *Nature* **2008**, *451*, 652−657.

(3) Liu, M.; Zhang, R.; Chen, W. *Chem. Rev.* **2014**, *114*, 5117-5160.

(4) Li, Y.; Zhou, W.; Wang, H.; Xie, L.; Liang, Y.; Wei, F.; Idrobo, J. C.; Pennycook, S. J.; Dai, H. *Nat. Nanotechnol.* **2012**, *7*, 394-400.

(5) Gong, K. P.; Du, F.; Xia, Z. H.; Durstock, M.; Dai, L. M. *Science* **2009**, *323*, 760-764.

(6) Yang, S.; Zhi, L.; Tang, K.; Feng, X.; Maier, J.; Mullen, K. *Adv. Funct. Mater.* **2012**, *22*, 3634-3640.

(7) Yang, Z.; Yao, Z.; Li, G.; Fang, G.; Nie, H.; Liu, Z.; Zhou, X.; Chen, X.; Huang, S. *ACS Nano* **2012**, *6*, 205-211.

(8) Zhang, C.; Hao, R.; Lian, H.; Hou, Y. *Nano Energy* **2013**, *2*, 88-97.

(9) Liang, J.; Jiao, Y.; Jaroniec, M.; Qiao, S. Z. *Angew. Chem.* **2012**, *124*, 11664-11668; *Angew. Chem. Int. Ed.* **2012**, *51*, 1-6.

(10) Liang, J.; Zheng, Y.; Chen, J.; Liu, J.; Hulicova-Jurcakova, D.; Jaroniec, M.; Qiao, S. Z. *Angew. Chem.* **2012**, *124*, 3958-3962; *Angew. Chem. Int. Ed.* **2012**, *51*, 3892-3896.

(11) Seredych, M.; Bandosz, T. J. *Carbon* **2014**, *66*, 227-233.

(12) Wang, L.; Ambrosi, A.; Pumera, M. *Angew. Chem.* **2013**, *125*, 14063-14066; *Angew. Chem. Int. Ed.* **2013**, *52*, 13818-13821.

(13) Silva, R.; Voiry, D.; Chhowalla, M.; Asefa, T. *J. Am. Chem. Soc.* **2013**, *135*, 7823-7826.

(14) Tao, G.; Zhang, L.; Chen, L.; Cui, X.; Hua, Z.; Wang, M.; Wang, J.; Chen, Y.; Shi, J. *Carbon* **2015**, *86*, 108-117.

(15) Chen, J.; Zhang, H.; Liu, P.; Li, Y.; Li, G.; An, T.; Zhao, H. *Carbon* **2015**, *92*, 339-347.

(16) Zhang, J.; Dai, L. *ACS Catal.* **2015**, *5*, 7244-7253.

(17) Daems, N.; Sheng, X.; Vankelecom, I. F. J.; Pescarmona, P. P. *J. Mater. Chem. A* **2014**, *2*, 4085-4110.

(18) Wu, J.; Yang, Z.; Li, X.; Sun, Q.; Jin, C.; Strasser, P.; Yang, R. *J. Mater. Chem. A* **2013**, *1*, 9889-9896.

(19) Wu, G.; More, K. L.; Johnston, C. M.; Zelenay, P. *Science* **2011**, *332*, 443-447.

(20) Watson, V. J.; Delgado, C. N.; Logan, B. E. *Environ. Sci. Technol.* **2013**, *47*, 6704-6710.

(21) Choi, C. H.; Park, S. H.; Woo, S. *ACS Nano* **2012**, *6*, 7084-7091.

(22) Deak, D.; Biddinger, E. J.; Luthman, K.; Ozkan, U. S. *Carbon* **2010**, *48*, 3637-3659.

(23) Zhong, M.; Kim, E. K.; McGann, J. P.; Chun, S. E.; Whitacre, J. F.; Jaroniec, M.; Matyjaszewski, K.; Kowalewski, T. *J. Am. Chem. Soc.* **2012**, *134*, 14846-14857.

(24) Seredych, M.; László, K.; Rodríguez-Castellón, E.; Bandosz, T. J. *J. Energy Chem.* **2016**, *25*, 236-245.

(25) Seredych, M.; László, K.; Bandosz, T. J. *ChemCatChem* **2015**, *7*, 2924-2931.

(26) Wang, S.; Zhang, L.; Xia, Z.; Roy, A.; Chang, D. W.; Baek, J.-B.; Dai, L. *Angew. Chem. Int. Ed.* **2012**, *51*, 4209-4212.

(27) Li, H.; Kang, W.; Wang, L.; Yue, Q.; Xu, S.; Wang, H.; Liu, J. *Carbon* **2013**, *54*, 249-257.

(28) Seredych, M.; Biggs, M.; Bandosz, T.J. *Micropor. Mesopor. Mater.* **2016**, *221*, 137-149.

(29) Seredych, M.; Rodriguez-Castellon, E.; Bandosz, T. J. *J. Mater. Chem. A* **2014**, *2*, 20164-20176.

(30) Wiggins-Camacho, J. D.; Stevenson, K. J. *J. Phys. Chem. C* **2011**, *115*, 20002-20010.

(31) D Yu, D.; Nagelli, E.; Du, F.; Dai, L. *J. Phys. Chem. Lett.* **2010**, *1*, 2165–2173.

(32) Dai, L.; Xue, Y.; Qu, L.; Choi, H. J.; Baek, J. B. *Chem. Rev.*, **2015**, *115*, 4823-4892.

(33) Kim, M., Kim, H.S., Yoo, SJ., Yoo, W. C., Sung, Y-E. *J. Mater. Chem. A.* **2017**, *5*, 4199-4206.

(34) Wang, L., Tang, Z., Yan, W., Yang, H.,Wang, Q., Chen, S. *ACS Appl. Mater. Interf.* **2016**, *8*, 20635-20641.

(35) Park, Y-C., Tkiwa, H., Kakinuma, K., Watanabe, M., Uchida, M. *J. Power. Sources* **2016**, *315*, 179-191.

(36) Yin, X, Lin, L., Chung, H.T., Komini Babu, S., Martinez, U., Purdy, G.M., Zelenay, P. *Presented at 231st ECS Meeting*, New Orleans, May 28-June 1, 2017.

(37) Seredych, M.; Szczurek, A.; Fierro, V.; Celzard, A.; Bandosz, T. J. *ACS Catal.* **2016**, *6*, 5618–5628.

(38) Jiang, Y., Yang, L., Sun, T., Zhao, J., Lyu, Z., Zhuo, O., Wang, X., Wu, Q., Ma, J., Hu, Z. *ACS Catalysis* **2015**, *5*, 6707-6712.

(39) Li, Y., Zhou, W., Wang, H., Xie, L., Liang, Y., Wei, F., Idrobo, J-C., Pennycook, S.J., Dai, H. *Nature Nanotechnol***. 2012**, *7*, 394-400.

(40) Szczurek, A.; Fierro, V.; Pizzi, A.; Stauber, M.; Celzard, A. *Carbon* **2013**, *65*, 214–227.

(41) Szczurek, A.; Fierro, V.; Pizzi, A.; Celzard, A. *Carbon* **2013**, *58*, 245-8.

(42) Hummers, W. S.; Offeman, R. E. *J. Am. Chem. Soc.* **1958**, *80*, 1339.

(43) Ferrero, G. A.; Preuss, K.; Fuertes, A. B.; Sevilla, M.; Titirici, M. M. *J. Mater. Chem. A* **2016**, *4*, 2581–2589.

(44) Jagiello, J.; Olivier, J. P. *Adsorption* **2013**, *19*, 777-783.

(45) Jagiello, J.; Bandosz, T. J.; Schwarz, J. A. *Carbon* **1994**, *32*, 1026-1028.

(46) Jagiello, J. *Langmuir* **1994**, *10*, 2778-2785.

(47) Figueiredo, J.; Pereira, M. F.; Freitas, M. M.; Órfão, J. J. *Carbon* **1999**, *37*, 1379–1389.

(48) Bandosz, T. J.; Ania, C. O. Surface chemistry of activated carbon and its characterization. In *Activated carbon surfaces in environmental remediation*, Bandosz TJ. Ed. Elsevier: Oxford, 2006, p 159-230.

(49) Feng, W. G.; Kwon, S.; Feng, X.; Borguet, E.; Vidic, R. D. *J. Environ. Eng.* **2006**, *132*, 292–300.

(50) Aik, S., Lee, J.W. *RCS Advances* 2015, *5*, 24661-24669.

(51) Qu, L.; Liu, Y.; Baek, J.-B.; Dai, L., *ACS Nano* **2010**, *4*, 1321-1326.

(52) Zurilla, R.; Sen, R.; Yeager, E., *J. Electrochem. Soc.* **1978**, *125*, 1103-1109.

(53) Guo, Z.; Xiao, Z., Ren, G., Xiao, G., Zhu, Y., Dai,, L., Jiang, L. *Nano Res***. 2016**, *9*, 1244-1255.

(54) Shi, Q, Wang, Y., Wang, Z.; Lei, Y., Wang, B., Wu, N., Han, C., Xie, S., Gou, Y. *Nano Res.* **2016**, *9*, 317-328.

(55) Fu, Y., Tian, C., Liu, F., Wang, L., Yan., H., Yang, B. *Nano Res.* **2016**, *9*, 3364-3376.

Captions to the Tables

Table 1. The parameters of porous structure calculated from nitrogen adsorption measurements using 2D-NLDFT model (S_{BET} – BET surface area; V_t – total pore volumes; V_{meso} – volume of mesopores; $V_{<0.7nm}$ and $V_{<1nm}$ – volume of pores less than 0.7 nm and 1 nm, respectively, V_{mic} – micropore volume), and affinity of carbons towards water vapor (in wt. %).

Table 2. Surface pH values, amounts of groups detected from potentiometric titration (in mmol g^{-1}), and content of elements on the surface detected by the XPS analysis (in at. %).

Table 3. The results of deconvolution of C 1*s*, O 1*s*, S 2*p* and N 1*s* core energy levels.

Captions to the Figures

Figure 1. Schematic view of the samples' modification procedure.

Figure 2. (a), (b) and (c) SEM images on the CM sample at different magnifications. (d) and (e) Cumulative and differential mercury intrusion curves, respectively.

Figure 3. Pore size distributions for the carbons studied calculated using 2D-NLDFT.

Figure 4. Proton-binding curves.

Figure 5. DTG curves in air for the samples tested.

Figure 6. Cyclic voltammograms measured using RRDE in 0.10 M KOH at scan rate of 5 mV s^{-1} for the materials studied.

Figure 7. Comparison of the onset potential (A), number of electron transfer (B) and the percentage of oxygen reduced to peroxide (C).

Figure 8. Kinetic current (A) and kinetic current density (B).

Figure 9. Chronoamperometry response for methanol crossover at the potential of the maximum of the oxygen reduction humps.

Figure 10. Stability of CM, CM-N, CM-S, CM-H, CMGO, CMGO-S, CMGO-H, and Pt/C in the ORR process over 1000 CV cycles.

TOC graphic

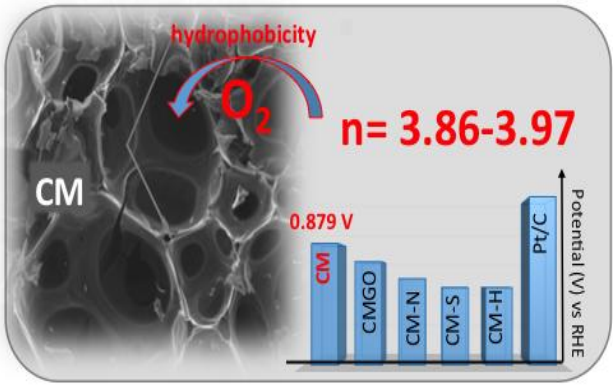
hydrophobicity
O2
n= 3.86-3.97
CM
0.879 V
CM
CMGO
CM-N
CM-S
CM-H
Pt/C
Potential (V) vs RHE